Quantum dynamics of a single molecule magnet on superconducting Pb(111)

Giulia Serrano, Lorenzo Poggini, Matteo Briganti, Andrea Luigi Sorrentino, Giuseppe Cucinotta, Luigi Malavolti, Brunetto Cortigiani, Edwige Otero, Philippe Sainctavit, Sebastian Loth, et al.

Quantum Dynamics of a Single Molecule Magnet on Superconducting Pb(111)

Giulia Serrano[1,2*], Lorenzo Poggini[1], Matteo Briganti[1], Andrea Luigi Sorrentino[1], Giuseppe Cucinotta[1], Luigi Malavolti[3], Brunetto Cortigiani[1], Edwige Otero[4], Philippe Sainctavit[4,5], Sebastian Loth,[3] Francesca Parenti[6], Anne-Laure Barra[7], Alessandro Vindigni[8], Andrea Cornia[6], Federico Totti[1], Matteo Mannini[1] and Roberta Sessoli[1*]

1. *Department of Chemistry "Ugo Schiff" and INSTM Research Unit, University of Florence, 50019 Sesto Fiorentino, Italy. roberta.sessoli@unifi.it*
2. *Department of Industrial Engineering, University of Florence, 50139 Florence, Italy. giulia.serrano@unifi.it*
3. *Max Planck Institute for Solid State Research, 70569 Stuttgart, Germany*
4. *Synchrotron SOLEIL, L'Orme des Merisiers, Saint Aubin BP48 91192 Gif-sur-Yvette Cedex, France*
5. *IMPMC, UMR7590 CNRS, Sorbonne Université, MNHN, 75005 Paris, France*
6. *Department of Chemical and Geological Sciences and INSTM Research Unit, University of Modena and Reggio Emilia, 41125 Modena, Italy*
7. *LNCMI-CNRS, Univ. Grenoble-Alpes, 38042 Grenoble cedex 9 France*
8. *Laboratorium für Festkörperphysik, ETH Zürich, Zürich, Switzerland*

Abstract

Magnetic materials interfaced with superconductors disclosed novel physical phenomena with high potentialities for quantum technologies. The use of molecules as magnetic components already showed great promises, but the vastity of properties offered by the molecular realm remains largely unexplored. Here we investigate a Single Molecule Magnet (SMM) deposited on the superconductive lead surface at sub-monolayer coverage. This combination reveals a strong influence of the superconductor (SC) on the spin dynamics of the SMM. It is shown that the superconductive transition to the condensate state switches the SMM from a blocked magnetization state to the resonant quantum tunnelling regime. This result opens perspectives for controlling SMM magnetism via SCs and for using SMMs as local probes of the superconducting state.

Introduction

Interfaces between superconducting and ferromagnetic materials are widely investigated for the richness of the novel physical phenomena they exhibit, which hold great potential in spintronics and quantum information technologies.[1] Among them, infinite magnetoresistance was observed in spin-valves embedding superconducting layers between ferromagnetic electrodes.[1] On the other hand, the intercalation of ferromagnetic layers in a Josephson junction introduces a tuneable shift in the phase between the two superconductors (SCs), allowing control of quantum circuits.[1] As far as molecular spins are concerned, scanning tunnelling spectroscopy in the proximity of flat paramagnetic molecules deposited on ultrathin superconducting layers provided examples of local quasiparticle excitations within the superconducting gap, giving rise to localized magnetic states known as Yu−Shiba−Rusinov (YSR) bound states.[2–4] Monolayers of paramagnetic molecules can also influence the critical temperature of a thin superconducting layer,[3,5,6] and exhibit increased spin lifetimes on superconducting bulk crystals.[7] However, the use of a superconducting substrate to manipulate the magnetism of molecular magnets is, to the best of our knowledge, unexplored. Among molecular magnets, molecules showing a directionally bistable magnetic moment are known as Single Molecule Magnets (SMMs). They combine a large molecular spin with an easy-axis magnetic anisotropy, which leads to an energy barrier opposing to the reversal of the magnetization.[8] Moreover, quantum phenomena in the spin dynamics make this class of nanomagnetic objects very appealing for spintronics and quantum computing.[9] Notably, Grover's algorithm has been implemented on a single nuclear spin by embedding a SMM in a nanojunction and using the electronic spin for the electric readout.[10]

Among the plethora of reported SMMs, those allowing the realization of a well-defined molecule-superconductor hybrid interface are limited. Tetrairon(III) complexes[11] (Fe_4) with a propeller shape (Figure 1a) constitute one of the few families of SMMs that have been studied in detail when deposited on a substrate.[12–15] Hybrid interfaces were obtained from solution,[12,13] as well as via thermal sublimation in UHV conditions.[14] In both cases the magnetic bistability was found to persist at sub-monolayer coverage, at variance with other SMM complexes,[16–18] thanks to the efficient protection of the magnetic core exerted by the ligand shell.

Here we report the investigation of a sub-monolayer of Fe_4 SMMs on lead, a type I superconductor (SC). We studied the structural and chemical properties of the Fe_4 monolayer by combining scanning tunnelling microscopy (STM) with spectroscopic techniques (*i.e.* Ultra-Violet and X-ray Photoelectron Spectroscopy, UPS and XPS, respectively) flanked by Density Functional Theory (DFT) calculations. We employed X-ray magnetic circular dichroism (XMCD) to observe the magnetic fingerprint of the molecular layer and investigate its magnetization dynamics inside the superconductive window. The results show that the magnetization dynamics of the SMMs is influenced by the SC transition to the condensate state.

Fe_4SMe on Pb (111): surface preparation and characterization

In the structure of Fe_4 SMMs, $[Fe_4(L^R)_2(dpm)_6]$, the magnetic core is held together by tripodal ligands $(L^R)^{3-} = [RC(CH_2O)_3]^{3-}$ located on either side of the molecular plane, whereas dipivaloylmethanido ligands (dpm^-) are found at the periphery (Figure 1a).[11]

The bridging oxygen atoms of the tripods promote antiferromagnetic interactions between the $s = 5/2$ spins of central and peripheral Fe^{3+} ions. The resulting ground state has total spin $S = 5$ and is well separated (ca. 55-65 K[19]) from the excited $S = 4$ states. The ground manifold is dominated by a moderate uniaxial magnetic anisotropy, $\hat{H}_{an} = D\hat{S}_z^2$, along the idealized C_3 molecular axis (z), which is oriented normal to the molecular plane. The anisotropy is of the easy-axis type with $D/k_B \sim -0.6$ K and creates an energy barrier $|D/k_B|\, S^2 \sim 15$ K. Magnetic bistability is thus observable in the hysteresis loops only at temperatures below 1 K. The loops present the butterfly shape typical of resonant quantum tunnelling of the magnetization (QTM) in zero field.[8]

As a key feature, Fe_4 complexes can be tailored by proper choice of R substituent on tripodal ligands while only marginally affecting magnetic properties. With R = Ph the molecules sublimate in UHV conditions but the bulky Ph group limits the formation of perfectly ordered monolayer.[14] On the contrary, Fe_4 SMMs with R = H, deposited using electrospray, adopt a flat adsorption geometry (*i.e.* with the plane defined by the Fe atoms parallel to the surface) and form ordered hexagonal layers.[20,21]

After careful screening of alternative substituents, we found that when R = CH_2SMe (see tripodal ligand in Figure 1a), the Fe_4 complex is compact enough to warrant the formation of a well ordered 2D lattice but also presents the necessary thermal stability to allow sublimation. The synthesis of the new proligand H_3L^{CH2SMe}, and of its tetrairon(III) complex (Fe_4SMe hereafter), are described in the Supplementary Note 1. Structural characterization by X-ray diffraction (see Supplementary Note 2) revealed the typical pseudo-three-fold symmetry. Characterization of the magnetic properties by DC and AC methods, flanked by high-frequency Electron Paramagnetic Resonance (EPR) spectroscopy, confirmed the dominating uniaxial magnetic anisotropy with spin Hamiltonian parameters in line with other derivatives of the same family (see Supplementary Note 3).

A Pb single crystal exposing the (111) face was selected as the substrate for molecular deposition. Lead behaves as a superconductor below the critical temperature (T_C) of 7.2 K and critical field (B_C) of 0.08 T.[22] In this field region, Fe_4 SMMs display enhanced magnetic bistability in normal conditions because resonant quantum tunnelling is suppressed.

The Fe_4SMe sub-monolayer on lead, Fe_4SMe/Pb(111), was prepared and characterized in controlled atmosphere ($P < 10^{-10}$ mbar). Before molecular deposition, the Pb(111) surface was cleaned by sputtering and annealing cycles. Molecules were deposited by thermal sublimation in order to obtain a sub-monolayer coverage, according to the preparation protocols provided in the Methods. STM images of the molecular film on Pb(111) with different magnifications are reported in Figure 2. Fe_4SMe molecules form molecular islands with a highly ordered hexagonal pattern with a periodicity of 1.7(2) nm, partially covering the Pb surface (a clean area is visible in the top-right side of Figure 2a). Detailed

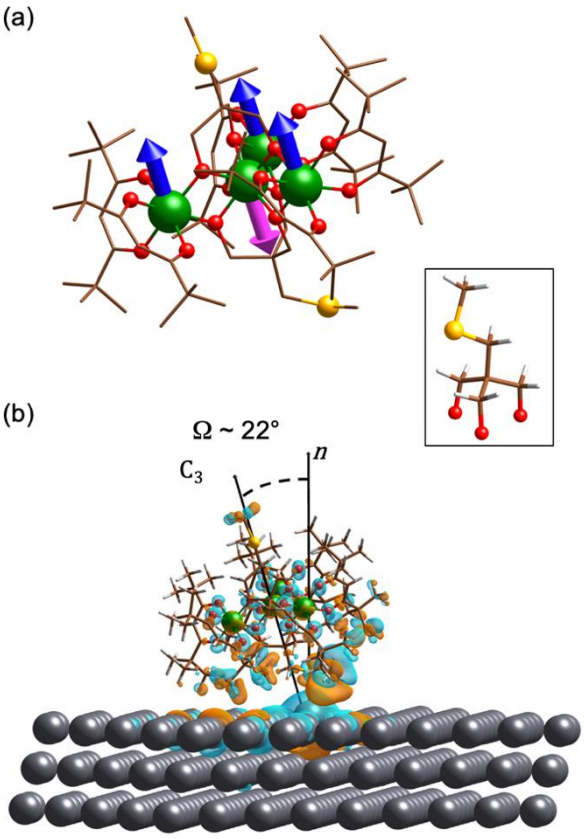

Figure 1 *(a) Structure of Fe_4SMe in the crystalline phase (atom colour code: green = Fe, red = O, yellow = S, brown = C). For clarity, the carbon backbone is drawn using capped sticks. Hydrogen atoms are not shown. Arrows indicate the arrangement of spin vectors in the ground S = 5 state. The tripodal ligand with the CH_2SMe substituent is depicted in the rectangular panel (white capped sticks = H). (b) Stable structure of Fe_4SMe on Pb(111) calculated by DFT, showing the deviation of magnetic easy axis (C_3) from the surface normal (n) and the computed difference electron density (the surfaces are drawn for a value of 0.0025 e bohr^{-3}). Cyan and orange colours correspond to reduced and increased electron densities, respectively, as compared with noninteracting components (Pb surface and Fe_4SMe).*

analysis of the STM height profiles of the surface before and after deposition of the Fe_4SMe layer is provided in the Supplementary Note 4. Different orientations of Fe_4SMe molecular pattern, specifically addressed in the Supplementary Figure 7 (Note 4), are observed and locally produce disordered areas at the borders of adjacent islands. Hexagonal packing in the molecular layer was also reported for R = H, favoured by the flat-lying adsorption geometry of this disk-like molecule.[20,21] In our case, the steric hindrance of the -CH_2SMe group produces a tilted adsorption geometry (similarly to complexes with R = Ph and $(CH_2)_5SAc$ on Au[14,23,24]), which complicates the interpretation of STM images. Indeed, a closer look at the molecular layer shown in Figure 2b indicates the presence of a superstructure of triangles formed by three molecular units. Triangles are packed with opposite orientation in a double row, or in a single row. In the latter

case, triangles alternate with a molecular unit (see Supplementary Note 4).

species in octahedral configuration (see Supplementary Note 6) and excludes the contamination by Fe^{II}.[27–30]

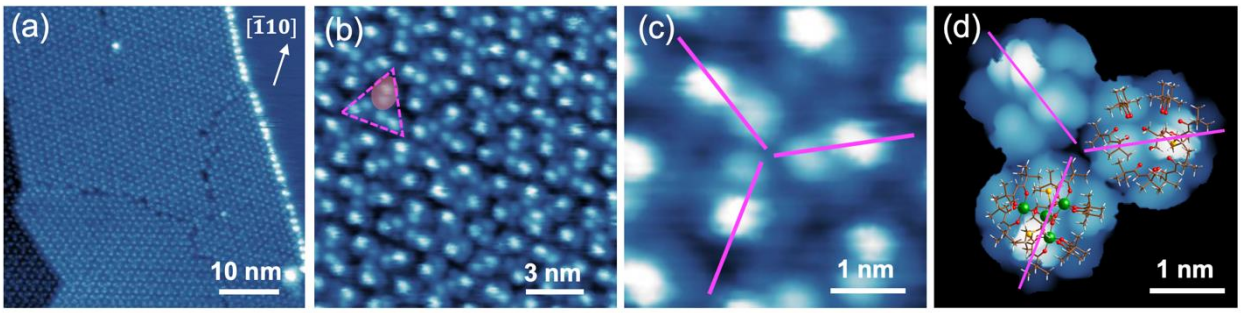

Figure 2 *(a-c) STM images (V_{bias} =2.6 V, I_{tunnel}=10 pA) of the Fe_4SMe sub-monolayer on Pb(111) at different magnifications. The dotted triangle in panel b highlights the molecular superstructure; a single molecular unit is indicated in shadow. (d) Simulated STM image of three molecules in the layer. In (c) and (d) pink lines mark the projections of molecular easy axes.*

In order to better understand the STM observations, we investigated the Fe_4SMe/Pb(111) interface by theoretical methods (detailed description in the Methods). One single Fe_4SMe molecule was optimized at the periodic DFT level of theory. In the relaxed geometry, the idealized three-fold axis (see Figure 1b) forms an angle Ω ~ 22° with the surface normal (*n*). This configuration is driven by vdW interactions of the Pb atoms with the sulphur atom and with the hydrogen atoms of two dipivaloylmethanido ligands positioned close to the surface. DFT also foresees a preferred atop interaction of S with a Pb atom, which is extracted by ca. 0.9 Å from the top layer. Calculations evidence a low energy adsorption configuration that indicates a physisorption process, being the lysis of the S-Me bond sterically hindered.[25,26]

The superstructure observed in the STM images can be reproduced through DFT modelling, taking into account three closely packed molecular units and allowing the structure to relax (see Methods). Supplementary Figure 10 (Note 5) shows the minimum energy configuration where molecules retain their easy axes at 22° with the surface normal, and the easy-axis projections on the surface are arranged at 120° intervals. In light of the simulated STM image of this structure (Figure 2d), we can interpret the experimental STM topography of Figure 2c. Each Fe_4SMe molecule appears as two main spots along the individual easy axis; the brighter corresponding to the -CH_2SMe group pointing outward and the other to the *tert*-butyl group belonging to the topmost dpm^- ligand. The other -CH_2SMe group cannot be directly identified from the experimental images, but it lies just beneath the latter spot. Additional lateral spots correspond to the rest of the molecular carbon backbone.

A chemical analysis of the Fe_4SMe/Pb(111) surface performed by XPS confirmed the integrity of the molecular layer after the deposition process (see semiquantitative analysis reported in the Supplementary Table 1 and 2, Note 6). In the C*1s* region, the relative intensities of the peaks due to aliphatic, aromatic and S-bound carbon atoms are in accordance with the molecular structure; the Fe*2p* region confirms the presence of Fe^{III}

The electronic structure of the molecular film was studied by UPS: the He (II) spectrum recorded on a 3 nm thick molecular film is shown in the Supplementary Note 7. The shape of the spectrum is compatible with literature reports on layers of similar Fe_4 complexes.[28,31] Furthermore, the comparison of the UPS spectrum with the corrected-total Density Of States (c-TDOS) and with the single-element contributions of the molecules to the TDOS allowed a careful assignment of each spectral feature (see Supplementary Note 7). Projected Density of States (pDOS) was also computed to get more insights on the molecule/surface interaction (see Supplementary Figures 11-13, Note 5). Being the Fermi region or relevance for superconductivity, we notice that the filled 3*d* bands (alpha component) of the iron ions start from -9 up to -1 eV with respect to the Fermi energy, E_f, while the empty ones are right above it (see Supplementary Figures 12 and 13, Note 5). Contributions of S, C, and O orbitals are also present in the range E_f±1eV (see Supplementary Figure 12, Note 5). To reveal any possible molecule-substrate hybridization that may result from the presence of S and Fe orbitals in this critical energy region, we computed the electron density difference between Fe_4SMe/Pb(111) and its separated components (Fe_4SMe and Pb substrate). Figure 1b shows that the largest difference is observed for the displaced Pb atom and the -SMe group; this indicates formation of a non-negligible covalent Pb-S interaction, leading to weak electronic hybridization. However, the spin density computed for the Fe_4SMe/Pb(111) interface (Supplementary Figure 14, Note 5) reveals no sizeable spin delocalization on the Pb atoms. This result is not surprising as the ligand shell efficiently shelters the Pb surface from the Fe^{3+} ions. We notice that a similarly negligible spin delocalization was observed for VOPc deposited on Pb with the vanadyl moiety pointing up, but the spin density increased significantly when the molecule was deformed by the STM tip.[3] Even if we cannot exclude such a possibility for Fe_4SMe/Pb(111), we consider it very unlikely due to the lack of spin density on molecular atoms close to the Pb surface.

Magnetic characterization of the molecular film

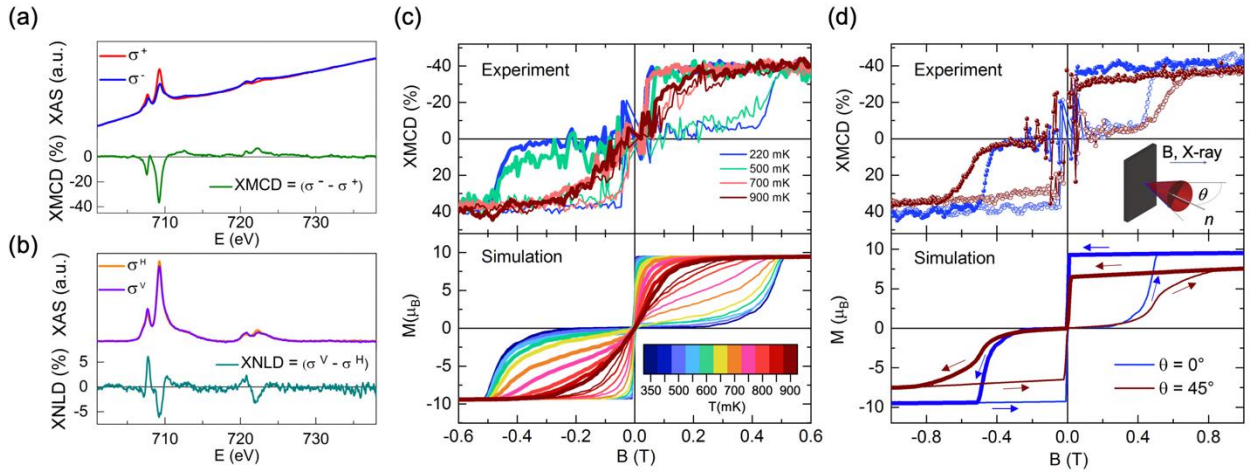

Figure 3. XMCD (a) and XNLD (b) spectra of Fe4SMe on Pb (111) at the Fe $L_{2,3}$ edge. XMCD signal (green) was obtained by recording XAS spectra with positive (red) and negative (blue) circular light polarization at 220 mK, 3 T and $\theta = 0°$. XNLD signal (cyan) was obtained from XAS spectra with linear vertical (violet) and horizontal (orange) light polarization at at 220 mK, 3 T and $\theta = 45°$. Temperature (c) and angular (d) dependence of experimental (top) and simulated (bottom) hysteresis loops. In the temperature dependence, experimental data were recorded by monitoring the field dependence of the XMCD signal at 709.2 eV at different temperatures (see legend) and normal incidence (v_{sweep}=0.01T/s). Curves are simulated using the Kinetic Monte Carlo approach (see text). In the angular dependence, experimental curves were recorded at θ = 0° (blue) and θ = 45° (dark red) at 220 mK. Simulations were performed considering the magnetic easy axis distributed along a cone (a magnified version of the inset is shown in Supplementary Figure 19). Thin (thick) lines and empty (filled) symbols represent upfield (downfield) hysteresis branches. Arrows help to visualize field scan direction in the simulated curves.

The magnetic characterization of the Fe_4SMe sub-monolayer on Pb(111) was carried out using X-ray synchrotron light and a ^{3}He-^{4}He dilution refrigerator to access the mK temperature range (see Methods).[32] X- ay Absorption Spectra (XAS) were measured at the Fe $L_{2,3}$ edges with the X-ray beam directed parallel to the applied magnetic field (B) and forming a variable angle θ with the surface normal (see inset in Figure 3d). Spectra were acquired at 3 T and 220 mK (nominally the lowest reachable temperature at the sample holder). At normal incidence ($\theta = 0°$) XAS spectra obtained with positive (σ^+, red) and negative (σ^-, blue) circular polarization show the expected shape for a Fe_4 complex (Figure 3a).[12–14] The XMCD signal (green curve), obtained in these conditions as $\sigma^- - \sigma^+$ and normalized (see Methods), shows a dominant (negative) peak at 709.2 eV with an intensity of about 40%. The intensity and line shape are distinctive of Fe_4 complexes, being a fingerprint of the antiparallel alignment between nearest-neighbouring spins in the ground state (Figure 1a).[12–14,33,34] A slightly lower intensity (~37%) is observed at $\theta = 45°$, as expected for molecules with a preferential orientation (see Supplementary Figure 17, Note 8).

X-ray light with linear polarization was used to further assess molecular orientation at the Pb(111) surface. XAS spectra were acquired at the Fe $L_{2,3}$ edges using linear vertical (σ^V, violet) and horizontal (σ^H, orange) polarization at $\theta = 45°$ (Figure 3b). The XNLD spectrum ($\sigma^V - \sigma^H$, cyan) is dominated by a dichroic signal at 709.2 eV, whose amplitude (about 6%) is greater than found in other monolayers of Fe_4 complexes.[13] It confirms a marked alignment of the molecules, in line with STM and DFT findings.

The dynamics of the magnetization of the Fe_4SMe layer on Pb(111) was studied at normal incidence ($\theta = 0°$) in the temperature range from 220 mK to 900 mK (Figure 3c). XAS signal was recorded at the energy of the maximum XMCD amplitude by sweeping the field continuously between -1.5/+1.5 T for right and left circular polarizations with a sweep rate v_{sweep} = 0.01 T/s (continuous mode, hereinafter). At 900 mK the hysteresis loop is practically closed; it opens progressively upon cooling and becomes almost temperature independent below 500 mK. This behaviour is typical of Fe_4 SMMs at the cross-over from a thermally activated relaxation mechanism to a tunnelling regime.[35]

Magnetic hysteresis was studied also as a function of the incidence angle θ at 220 mK (Figure 3d). The hysteresis curves are characterized by efficient QTM at zero field ("butterfly shape"), as found in other monolayer deposits of Fe_4 complexes.[13,14] At normal incidence, the hysteresis closes rather abruptly at about ± 0.45 T in correspondence to the first field-induced level crossing, *i.e.* where the $m_s = \pm 5$ and $m_s = \mp 4$ levels are degenerate, and QTM is enhanced.[11,36] By contrast, at $\theta = 45°$ we observe a gradual change of the magnetization from 0.45 T to 0.70 T. Geometrical arguments can explain this finding. According to DFT results, molecular easy axes are tilted by $\Omega \sim 22°$ from the surface normal and, in first approximation, distributed on the surface of a cone with half-angle equal to Ω (see inset of Figure 3d). It follows that at $\theta = 0°$ all molecules have the same orientation with respect to the magnetic field. Level crossing thus occurs exactly at the same field in all molecules, and a sharp step in the magnetization is observed. On the contrary, at $\theta = 45°$, the angle between the external field and the molecular easy axis spans the interval $45° \pm \Omega$, *i.e.*

from 67° to 23°. Since level crossing moves to higher fields with increasing angles, the hysteresis closes over a wider field range.

Hysteresis loops were simulated by placing the molecular easy axes at 22° from the surface normal and optimizing the spin Hamiltonian parameters to the values reported in the Supplementary Note 9. The easy axis projections on the Pb(111) surface were distributed over 12 possible orientations with respect to the [$\bar{1}$10] direction, in agreement with STM data (see

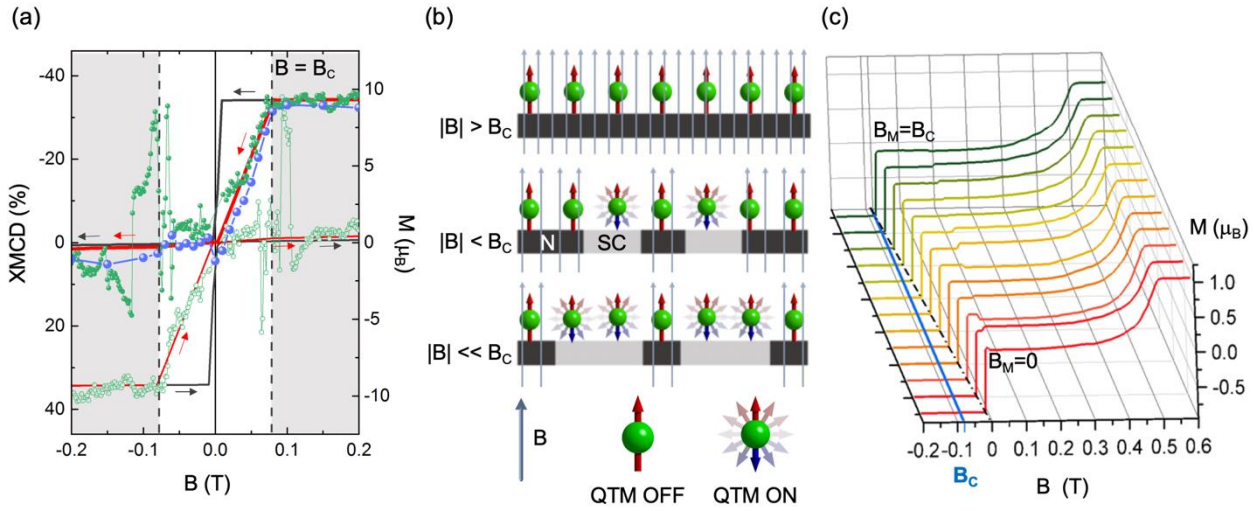

Figure 4. (a) Experimental hysteresis loops acquired close to B_C (0.08T) at θ = 0° and 220 mK: green circles represent the hysteresis acquired by the continuous method (v_{sweep} = 0.0025 T/s) while blue circles refer to spot XMCD values (spot method) recorded after magnetizing the sample at 1 T at each point (detailed explanation is given in the text). Hysteresis loops simulated without considering the superconducting substrate (grey line) and introducing the effect of the superconducting substrate in the intermediate state (red line) are also shown. Thin (thick) lines and empty (filled) symbols represent upfield (downfield) hysteresis branches. Arrows help to visualize field scan direction in the simulated curves. (b) Scheme of the interaction of SMMs with the superconducting substrate during the SC transition to the intermediate state ($|B| < B_C$). For $|B| > B_C$ molecular spin is aligned along the magnetic field direction; $|B| = B_C$ represents the nominal transition of the type I superconductor to the condensate state. From B_C to zero field, growing substrate areas enter in the complete Meissner state (grey) thus excluding the external magnetic field (B_{loc} =0). Fe_4SMe molecules interacting with these regions feel a magnetic field drop to zero allowing them to bypass the anisotropy barrier via quantum tunnelling. (c) Simulated magnetization curves (upfield branch of the hysteresis loop) for molecules experiencing the superconducting transition of lead at different B_M and thus different times in the hysteresis cycle. Simulated hysteresis loop, red line in panel a, was obtained taking into account a convolution of these hystereses (see text).

Simulation of the hysteresis loops

Simulation of the Fe_4SMe magnetic hysteresis was performed starting from the spin Hamiltonian of the ground $S=5$ state and computing the transition probabilities between the different sublevels.[13] In order to improve the efficiency of the simulation, the time dependence of the magnetization was evaluated by the kinetic Monte Carlo method (see Supplementary Note 9) rather than the previously employed direct integration of the master equation.[13] Thermally-activated processes were treated considering the spin-phonon coupling explicitly, within the approximations presented in Ref. 8. An additional heuristic term was added to the transition rates to account for pure tunnelling between almost degenerate levels. The resulting master equation was integrated using the kinetic Monte-Carlo method to evaluate the time-dependent magnetization (see Supplementary Note 9). The use of (variable-step) kinetic Monte Carlo, based on stochastic time increments, has the advantage of providing comparable accuracy with less computational resources compared to direct integration,[13] which requires an appropriate *a priori* choice of the integration (fixed) time step.

Supplementary Figure 7, Note 4). However, the assumption of a continuous distribution gave virtually identical results. The close agreement of the simulated and experimental curves over the whole temperature range here explored (see Figure 3c) indicates the reliability of this approach. Differences in the hysteresis loop for different incidence angles (Figure 3d) are also nicely reproduced.

SMMs dynamics inside the superconducting window of lead

We now focus on the dynamics of the magnetization of Fe_4SMe in the field range in which the substrate is superconductor ($|B| < B_C$). Figure 4a shows an enlargement of the low field region of the hysteresis loop at $\theta = 0°$ and 220 mK (green circles), acquired at a lower field sweep rate (0.0025 T/s) than in Figure 3 (0.01 T/s) in order to increase the data resolution. Starting from high fields, when the applied field enters in the superconducting window ($B < B_C$) the XMCD signal decreases, deviating significantly from the predicted squared behaviour around zero field (grey line) and from the observed response of similar complexes on non-superconductive substrates[32] (a detailed comparison is

available in Supplementary Figure 18, Note 8). It can be noticed that the noise level in the experimental data increases significantly when the applied field exits from the superconducting window. Rapid variations of the magnetic induction around zero field are known to affect the efficiency of the photoelectrons leaving the sample and thus to influence the signal detection in the TEY mode (see Methods). Flux noise effects were also detected in superconducting circuits and attributed to the presence of O_2 molecules.[37,38] However, a possible explanation for the asymmetry of the noise herein observed is that the magnetic induction of the molecular film has a mitigating effect on the photoelectrons. When the substrate enters the superconducting phase, the molecular layer is fully magnetized, and its magnetization gradually vanishes towards zero field. As the field is reversed and exits the superconducting window, then, the molecular layer is fully demagnetized, leading to an abrupt change in the local induction felt by the photoelectrons.

To minimize this effect, the XAS signal was recorded by switching the X-ray polarization at each sampled magnetic field. The field was ramped back to 1 T before measuring each point of the hysteresis in order to maintain a sweep rate similar to the continuous mode. The blue circles in Figure 4a represent the hysteresis data acquired in this "spot" mode. Also in this case, the Fe_4SMe magnetization decays below B_C, clearly evidencing that the SMMs in the monolayer experience the local field (B_{loc}) generated by the superconductor.

The approximately linear decrease of the magnetization observed below B_C is, in fact, in agreement with the transition of a type I superconductor to the intermediate state. In this state superconducting and normal (N) regions coexist in the metal.[39] In a simplified model, *i.e.* assuming the demagnetization factor equals to one, the superconducting fraction (f_S) increases linearly by lowering $|B|$ according to $f_s \sim 1-|B|/B_C$.[39]

Regions of the superconductor entering the complete Meissner state (light grey areas in Figure 4b) expel the applied magnetic field, pushing the field flux lines in the neighbouring N regions (dark grey in Figure 4b), where the magnetic field is pinned to the B_C value.[39] The relative amounts of SC and N regions vary with the applied magnetic field, as sketched in Figure 4b. Thus, each region of the superconductor experiences the transition to the Meissner state at different values of the applied field, ranging from B_C to zero field.

This scenario is expected to represent also our experimental conditions. Magneto-optical studies, indeed, revealed the presence of the intermediate state in disk-shaped lead crystals with similar size to ours.[40,41] The topology of the domains depends on the shape of the sample and the applied magnetic field. Their dimension ranges from micrometric to sub-mm size.[40,41] Being the size of the X-ray spot about 1 mm in diameter, the XMCD signal averages the response of SMMs lying on N and SC regions.

For $B < B_C$, SMMs experience a B_{loc} generated by the superconductor: those in the proximity of a normal region feel $B_{loc} \sim B_C$ until that region enters into the Meissner state, B_M being the applied field at which this occurs. At this point, the molecules suddenly feel a local field $B_{loc} \sim 0$, and magnetic relaxation by QTM becomes possible.

To reproduce the hysteresis curve, we simulated a set of hystereses assuming different B_M values (Figure 4c), so as to describe SMMs that feel an abrupt transition from B_C to zero field at different times during the field scan. Taking into account the fractions of the substrate that experience different B_M values, and assuming a homogenous distribution of SMMs on the surface, we obtained the hysteresis curve shown as a red line in Figure 4a. In the superconducting window, the demagnetization of the Fe_4SMe layer is calculated to occur linearly with the field, in good agreement with the experimental data. It is also interesting to analyse the branch of the hysteresis measured by increasing the field amplitude but with opposite polarity. Both experimental and calculated curves are close to zero. Indeed, Fe_4SMe SMMs cannot be magnetized when the underlying Pb region exits the Meissner state, and the local field switches back to B_C. At this field, resonant quantum tunnelling is suppressed, and the magnetization is practically blocked over the time scale of the hysteresis. The absence of a linear trend in this portion of the hysteresis allows excluding the presence of species behaving like normal paramagnets.

Outlook

The unprecedented combination of two materials, which are archetypes of two very different classes, *i.e.* superconductors and SMMs, has here provided the proof of principle of a novel mechanism for SMMs magnetization switching and SC sensing. The formation of the intermediate state in a type I SC induces the transition of Fe_4SMe SMMs from the blocked magnetization to the resonant quantum tunnelling regime. Such a transition is promoted by the external field cancellation associated with the Meissner effect.

Fundamental for this achievement was (i) the chemical design of an evaporable Fe_4 SMM forming an ordered monolayer on the Pb substrate and (ii) the observation of hysteresis curves at sub-kelvin temperatures by XMCD. It is noteworthy that this surface-sensitive technique has been seldom employed to investigate superconductivity, as it is unable to detect the diamagnetic state of a SC. The few available XMCD studies have required the deposition of ferromagnetic overlayers.[42] At variance with ferromagnets, SMMs have the advantage of a non-cooperative hysteretic behaviour. Thus, when deposited on SC surfaces, SMMs are a sensitive local tool to monitor magnetic flux distribution of relevance for more complex domain structures, such as those observed in type II or 2D superconductors. For the latter, we can also expect to have a mutual magnetic influence through space, *i.e.* the magnetic flux generated by the SMM can locally affect the SC. Particularly relevant for the scientific community would be the investigation of the SMM/SC interface by scanning probe techniques with magnetic sensing capabilities and high spatial resolution.

Equally relevant is the possibility to locally switch the SMM magnetization dynamics biasing the magnetic field at the superconductor transition. This

effect is highly interesting for quantum information technologies and is expected to be particularly pronounced for lanthanoid-based SMMs, whose magnetization relaxation time can be enhanced by several orders of magnitude[43] in zero field.

Experimental Methods

Fe_4SMe (isolated in crystalline form as the hemidiethylether solvate) was synthesized and chemically characterized at the University of Modena and Reggio Emilia. A detailed description of the synthetic procedure and selected characterization data are provided in the Supplementary Information, Note 1.

The Pb(111) crystal was purchased from the Surface Preparation Laboratory – SPL (disk-shaped, 4 mm of diameter and 3 mm thickness). Surface preparation and characterization were performed at the University of Florence. The Pb(111) surface was prepared by cycles of Ar sputtering (1 keV energy) and annealing at 470 K in Ultra High Vacuum (UHV) and controlled by XPS and STM measurements. Molecular deposition was performed by thermal sublimation in UHV. Crystals of Fe_4SMe were crushed into a powder and inserted in a resistively heated quartz crucible. The powder was purified by repeated thermal treatment cycles to remove solvent residuals. The deposition was carried out at a temperature of about 490 K measured by a K-thermocouple in direct contact with the powder. The deposition rate was monitored by a quartz crystal microbalance placed in front of the crucible. The STM characterization was carried out by an Omicron Variable-Temperature STM, where the sample was cooled down to 30 K by a liquid helium flux. Diffraction pattern images were acquired by Omicron Spectaleed rear view LEED optics. XPS measurements were performed with a micro-focused monochromatic Al K-alpha radiation source ($h\nu$ = 1486.7 eV), model SPECS XR-MS Focus 600, and a multichannel detector electron analyser, model SPECS Phoibos 150 1DLD. XPS spectra were measured in normal emission with the X-ray source mounted at an angle of 54.44° with respect to the analyser and using a pass energy of 40 eV. Spectra were calibrated using the Pb$4f_{7/2}$ component at 136.9eV.[44] The spectra were fitted using a linear background and single peak components were deconvoluted by a mixed Gaussian and Lorentzian function. Spectra were analysed using the CasaXPS software.

UPS was carried out using a He (II) line (with an energy of 40.8 eV) by non-monochromatized gas discharge lamp (VG Scientific 22-101). The analyser was the same used for XPS with a pass energy of 10 eV and an entrance and an exit slit of 3×20 mm. A fixed bias of −30 V was applied to the sample to ensure the detection of all the photoelectrons.

XAS, XMCD, and XNLD measurements were carried out at the DEIMOS beamline (SOLEIL synchrotron, France) using the novel Dichro50 setup working in the mK temperature range.[32] Samples were prepared in Florence following the above reported procedures and transferred to the beamline facilities using a UHV suitcase equipped with a D100 SAES Nextorr Neg - Ion Combination Pump that guaranteed a pressure $P < 10^{-10}$ mbar during the transport. All the steps from sample preparation to synchrotron measurements were accomplished without breaking the vacuum connection ($P < 10^{-9}$ mbar). XAS spectra were acquired in Total Electron Yield (TEY) mode.[45] The XMCD signals were normalized with respect to the L_3 edge-jump of $(\sigma^+ + \sigma^-)/2$ and expressed in percentage.[15] The XNLD signals were normalized with respect to the L_3 edge-jump of the isotropic spectrum (*i.e.* $1/3\ \sigma^V + 2/3\ \sigma^H$ when $\theta = 45°$) and expressed in percentage.

Computational Methods

All the periodic density functional theory calculations (pDFT) were performed with CP2K quantum chemistry software.[46] Gaussian plane waves formalism (GPW)[47] is employed to solve the eigenvalue problem. Norm-conserving Goedecker-Tetter Hutter (GTH) pseudopotentials,[48] along with double zeta basis set with polarization functions (DZVP-MOLOPT-SR)[48] were employed for all atoms. The cut-off energy for the plane-wave auxiliary basis set was set to 400 Ry. Meta-GGA RevPBE functional[49,50] with empirical dispersion correction RVV10[51] was used throughout all the calculations. Constant electronic smearing of 1500 K was applied to consider the metal character of the slab. The threshold for the atomic forces during the geometry optimization runs was set to 0.003 Hartree/a_0, where a_0 is the Bohr radius (1 Hartree/a_0 = 8.2387234983(12) × 10^{-8} N), while during the single SCF step the convergence criterion was set to a wavefunction gradient of 1×10^{-6}.

Two different kinds of geometry optimizations were performed: the optimization of a single Fe_4SMe molecule (A) and the optimization of the adduct made by three Fe_4SMe molecules (B). The dimensions of the periodic cell were set to 31.5 × 30.3 × 60 Å for A and to 45.5 × 42.42 × 60 Å for B, in order to avoid interactions between replicas along both x and y directions and between slabs along the z directions. The starting guess geometry for optimization B was the final geometry obtained from optimization A. The latter was indeed replicated by a rigid rotation of 120° and 240° along the normal to the surface.

A total spin value corresponding to a broken state[52] with M_S = 5 was chosen, with the central Fe^{III} ion antiferromagnetically coupled with the three peripheral ones.

The Pb(111) surface was modelled with three slabs, each one made of 9 × 10 Pb atoms for A and of 14 × 13 for B. The bottom layer was kept fixed during all geometry optimizations, while the others were left free to relax. Such Pb(111) surface model was previously validated in Ref. 3 by some of us according to Ref 53.

Author contribution

GS, LP, ALS, GC and LM performed the synchrotron experiments with the assistance of EO, PS and MM. LP, GS and ALS prepared and characterized the hybrid

interface. MB and FT performed the DFT studies. FP and AC prepared and structurally characterized the Fe_4SMe SMM. RS, ALB, and AC performed its bulk phase magnetic characterization. AV developed the kinetic Monte Carlo method and contributed with GS and RS to the simulation of the XMCD magnetic data. AC, FT, MM, and RS supervised the activities of the project. All authors contributed to the discussion and preparation of the manuscript.

Data Availability

All relevant data, including ASCII files of all the recorded spectra and XYZ files for STM images, are available from the authors on request.

References

1. Linder, J. & Robinson, J. W. A. Superconducting spintronics. *Nat. Phys.* **11**, 307–315 (2015).
2. Franke, K. J., Schulze, G. & Pascual, J. I. Competition of Superconducting Phenomena and Kondo Screening at the Nanoscale. *Science.* **332**, 940–944 (2011).
3. Malavolti, L. *et al.* Tunable Spin-Superconductor Coupling of Spin ½ Vanadyl-Phthalocyanine Molecules. *Nano Lett.* **18**, 7955–7961 (2018).
4. Heinrich, B. W., Pascual, J. I. & Franke, K. J. Single magnetic adsorbates on s-wave superconductors. *Prog. Surf. Sci.* **93**, 1–19 (2018).
5. Kezilebieke, S., Dvorak, M., Ojanen, T. & Liljeroth, P. Coupled Yu–Shiba–Rusinov States in Molecular Dimers on $NbSe_2$. *Nano Lett.* **18**, 2311–2315 (2018).
6. Farinacci, L. *et al.* Tuning the Coupling of an Individual Magnetic Impurity to a Superconductor: Quantum Phase Transition and Transport. *Phys. Rev. Lett.* **121**, 196803 (2018).
7. Heinrich, B. W., Braun, L., Pascual, J. I. & Franke, K. J. Protection of excited spin states by a superconducting energy gap. *Nat. Phys.* **9**, 765–768 (2013).
8. Gatteschi, D., Sessoli, R. & Villain, J. *Molecular Nanomagnets*. **54**, (Oxford University Press 2006, 2006).
9. Sanvito, S. *et al.* Molecular spintronics. *Chem. Soc. Rev.* **40**, 3336–55 (2011).
10. Godfrin, C. *et al.* Operating Quantum States in Single Magnetic Molecules: Implementation of Grover's Quantum Algorithm. *Phys. Rev. Lett.* **119**, 187702 (2017).
11. Cornia, A., Mannini, M., Sessoli, R. & Gatteschi, D. Propeller-Shaped Fe_4 and Fe_3 M Molecular Nanomagnets: A Journey from Crystals to Addressable Single Molecules. *Eur. J. Inorg. Chem.* **2019**, 552–568 (2019).
12. Mannini, M. *et al.* Magnetic memory of a single-molecule quantum magnet wired to a gold surface. *Nat. Mater.* **8**, 194–197 (2009).
13. Mannini, M. *et al.* Quantum tunnelling of the magnetization in a monolayer of oriented single-molecule magnets. *Nature* **468**, 417–421 (2010).
14. Malavolti, L. *et al.* Magnetic Bistability in a Submonolayer of Sublimated Fe_4 Single-Molecule Magnets. *Nano Lett.* **15**, 535–541 (2015).
15. Totaro, P. *et al.* Tetrairon(III) Single-Molecule Magnet Monolayers on Gold: Insights from ToF-SIMS and Isotopic Labeling. *Langmuir* **30**, 8645–8649 (2014).
16. Margheriti, L. *et al.* X-Ray Detected Magnetic Hysteresis of Thermally Evaporated Terbium Double-Decker Oriented Films. *Adv. Mater.* **22**, 5488–5493 (2010).
17. Serrano, G. *et al.* Magnetic bistability of TbPc2 submonolayer on a graphene/SiC(0001) conductive electrode. *Nanoscale* **10**, 2715–2720 (2018).
18. Malavolti, L. *et al.* Magnetism of $TbPc_2$ SMMs on ferromagnetic electrodes used in organic spintronics. *Chem. Commun.* **49**, 11506 (2013).
19. Carretta, S. *et al.* Intra- and inter-multiplet magnetic excitations in a tetrairon(III) molecular cluster. *Phys. Rev. B* **70**, 214403 (2004).
20. Erler, P. *et al.* Highly Ordered Surface Self-Assembly of Fe_4 Single Molecule Magnets. *Nano Lett.* **15**, 4546–4552 (2015).
21. Gragnaniello, L. *et al.* Uniaxial 2D Superlattice of Fe_4 Molecular Magnets on Graphene. *Nano Lett.* **17**, 7177–7182 (2017).
22. Chanin, G. & Torre, J. P. Critical-Field Curve of Superconducting Lead. *Phys. Rev. B* **5**, 4357–4364 (1972).
23. Fernandez Garcia, G., Lunghi, A., Totti, F. & Sessoli, R. The disclosure of mesoscale behaviour of a 3d-SMM monolayer on Au(111) through a multilevel approach. *Nanoscale* **10**, 4096–4104 (2018).
24. Lunghi, A., Iannuzzi, M., Sessoli, R. & Totti, F. Single molecule magnets grafted on gold: magnetic properties from ab initio molecular dynamics. *J. Mater. Chem. C* **3**, 7294–7304 (2015).
25. Rajaraman, G., Caneschi, A., Gatteschi, D. & Totti, F. A periodic mixed gaussians–plane waves DFT study on simple thiols on Au(111): adsorbate species, surface reconstruction, and thiols functionalization. *Phys. Chem. Chem. Phys.* **13**, 3886 (2011).
26. Rajaraman, G., Caneschi, A., Gatteschi, D. & Totti, F. A DFT exploration of the organization of thiols on Au(111): a route to self-assembled monolayer of magnetic molecules. *J. Mater. Chem.* **20**, 10747 (2010).
27. Rigamonti, L. *et al.* Enhanced Vapor-Phase Processing in Fluorinated Fe 4 Single-Molecule Magnets. *Inorg. Chem.* **52**, 5897–5905 (2013).
28. Lanzilotto, V. *et al.* The Challenge of Thermal Deposition of Coordination Compounds: Insight into the Case of an Fe_4 Single Molecule Magnet. *Chem. Mater.* **28**, 7693–7702 (2016).
29. Mekki, A., Holland, D., McConville, C. F. & Salim, M. An XPS study of iron sodium silicate glass surfaces. *J. Non. Cryst. Solids* **208**, 267–276 (1996).

30. Yamashita, T. & Hayes, P. Analysis of XPS spectra of Fe^{2+} and Fe^{3+} ions in oxide materials. *Appl. Surf. Sci.* **254**, 2441–2449 (2008).
31. Ninova, S. *et al.* Valence electronic structure of sublimated Fe_4 single-molecule magnets: an experimental and theoretical characterization. *J. Mater. Chem. C* **2**, 9599–9608 (2014).
32. Kappler, J.-P. *et al.* Ultralow-temperature device dedicated to soft X-ray magnetic circular dichroism experiments. *J. Synchrotron Rad* **25**, 1727–1735 (2018).
33. Mannini, M. *et al.* Spin Structure of Surface-Supported Single-Molecule Magnets from Isomorphous Replacement and X-ray Magnetic Circular Dichroism. *Inorg. Chem.* **50**, 2911–2917 (2011).
34. Perfetti, M. *et al.* Grafting Single Molecule Magnets on Gold Nanoparticles. *Small* **10**, 323–329 (2014).
35. Cornia, A. *et al.* Energy-barrier enhancement by ligand substitution in tetrairon(III) single-molecule magnets. *Angew. Chemie - Int. Ed.* **43**, 1136–1139 (2004).
36. Vergnani, L. *et al.* Magnetic Bistability of Isolated Giant-Spin Centers in a Diamagnetic Crystalline Matrix. *Chem. - A Eur. J.* **18**, 3390–3398 (2012).
37. Kumar, P. *et al.* Origin and Reduction of 1/f Magnetic Flux Noise in Superconducting Devices. *Phys. Rev. Appl.* **6**, 041001 (2016).
38. Wang, H. *et al.* Candidate Source of Flux Noise in SQUIDs: Adsorbed Oxygen Molecules. *Phys. Rev. Lett.* **115**, 077002 (2015).
39. Poole, C. P., Farach, H. A., Creswick, R. J. & Prozorov, R. *Superconductivity*. (Elsevier Science, 2014).
40. Prozorov, R. Equilibrium Topology of the Intermediate State in Type-I Superconductors of Different Shapes. *Phys. Rev. Lett.* **98**, 257001 (2007).
41. Prozorov, R., Giannetta, R. W., Polyanskii, A. A. & Perkins, G. K. Topological hysteresis in the intermediate state of type-I superconductors. *Phys. Rev. B* **72**, 212508 (2005).
42. Ruoß, S., Stahl, C., Weigand, M., Schütz, G. & Albrecht, J. High-resolution dichroic imaging of magnetic flux distributions in superconductors with scanning x-ray microscopy. *Appl. Phys. Lett.* **106**, 022601 (2015).
43. Car, P.-E. *et al.* Giant field dependence of the low temperature relaxation of the magnetization in a dysprosium(iii)–DOTA complex. *Chem. Commun.* **47**, 3751 (2011).
44. Bozack, M. J. & Bryant, K. W. Elemental Lead by XPS. *Surf. Sci. Spectra* **1**, 324–327 (1992).
45. Nakajima, R., Stöhr, J. & Idzerda, Y. U. Electron-yield saturation effects in ***L***-edge x-ray magnetic circular dichroism spectra of Fe, Co, and Ni. *Phys. Rev. B* **59**, 6421–6429 (1999).
46. Hutter, J., Iannuzzi, M., Schiffmann, F. & VandeVondele, J. cp2k: atomistic simulations of condensed matter systems. *Wiley Interdiscip. Rev. Comput. Mol. Sci.* **4**, 15–25 (2014).
47. LIPPERT, B. G. & PARRINELLO, J. H. and M. A hybrid Gaussian and plane wave density functional scheme. *Mol. Phys.* **92**, 477–488 (1997).
48. Krack, M. Pseudopotentials for H to Kr optimized for gradient-corrected exchange-correlation functionals. *Theor. Chem. Acc.* **114**, 145–152 (2005).
49. Zhang, Y. & Yang, W. Comment on "Generalized Gradient Approximation Made Simple". *Phys. Rev. Lett.* **80**, 890–890 (1998).
50. Perdew, J. P., Burke, K. & Ernzerhof, M. Generalized Gradient Approximation Made Simple. *Phys. Rev. Lett.* **77**, 3865–3868 (1996).
51. Sabatini, R., Gorni, T. & de Gironcoli, S. Nonlocal van der Waals density functional made simple and efficient. *Phys. Rev. B* **87**, 041108 (2013).
52. Bencini, A. & Totti, F. A Few Comments on the Application of Density Functional Theory to the Calculation of the Magnetic Structure of Oligo-Nuclear Transition Metal Clusters. *J. Chem. Theory Comput.* **5**, 144–154 (2009).
53. Caneschi, A., Gatteschi, D. & Totti, F. Molecular magnets and surfaces: A promising marriage. A DFT insight. *Coord. Chem. Rev.* **289**–**290**, 357–378 (2015).